Effect of annealing temperature on microstructure and mechanical properties of nano-Y_2O_3 mediated selective laser melting TA15 alloy

Shuang Hu[1,2], Lei Zhang[1,2], Tian-xin Li[1,2], Chao-wen Huang[1,2], Rui Ma[1,2], Xian-li Ren1,2, *Ming-pan Wan[1,2], **Xing Ran[3]

1. College of Materials and Metallurgy, Guizhou University, Guiyang, 550025, China

2. National Local Co-construction Engineering Laboratory for high performance metal structure Material and Manufacture Technology, Guiyang, 550025, China

3. AVIC Heavy Machinery Co. Ltd., Guiyang, 550005, China

*Corresponding author address: mpwan@gzu.edu.cn (Mingpan Wan)

**Corresponding author address: ranxing1001@163.com (Xing Ran)

Abstract: Additive manufacturing of titanium alloys offers significant advantages such as high precision, reduced material waste, and enhanced design flexibility. However, post-processing is still necessary to optimize the microstructure and properties. The effect of annealing temperature (500~900°C) on the microstructure and mechanical properties of selective laser melting (SLM)-fabricated TA15 titanium alloy reinforced with nano-Y_2O_3 particles was systematically investigated. Phase evolution, including α′-martensite decomposition, β-phase coarsening, and nano-twin dynamics, was analyzed via SEM, EBSD, and TEM. At 500°C, partial α′ decomposition produced a mixed α+α′+β structure, elevating yield strength (YS) and ultimate tensile strength (UTS) by 9% and 7.6%, respectively, but reducing elongation (EL) to 5.8%. Complete α′→α+β transformation at 600°C achieved optimal UTS (1318 MPa) and EL (7.6%), attributed to refined nano-twins and stabilized β-phase distribution. Temperatures exceeding 600°C induced β-phase coarsening and nano-twin dissolution, reducing strength (UTS: 1097 MPa at 900°C) while enhancing ductility (EL: 15.6%). Y_2O_3 nanoparticles suppressed β-phase precipitation and delayed nano-twin decomposition. Fracture modes transitioned from cleavage-dominated to ductile-brittle with increasing temperature. The 600°C-annealed alloy demonstrated superior strength-ductility synergy compared to conventional TA15, highlighting Y_2O_3's dual role in stabilizing interfaces and tailoring microstructural evolution. This work provides insights into designing high-performance oxide-dispersion-strengthened (ODS) titanium alloys for aerospace applications through controlled annealing and oxide-mediated phase engineering.

Keywords: Selective laser melting; TA15 titanium alloy; Annealing temperature; Nano-Y_2O_3; Microstructure; Tensile properties

1 Introduction

The near α TA15 titanium alloy, renowned for its high specific strength, exceptional corrosion resistance, and high-temperature performance, has become a pivotal structural material in the aerospace industry[1-4]. Traditional manufacturing processes for TA15 titanium alloy,predominantly forging and machining, are inefficient and wasteful when fabricating complex-shaped components[5-7]. The advent of additive manufacturing technologies, such as selective laser melting (SLM) and laser powder bed fusion (LPBF), offers innovative solutions to these challenges[8, 9]. These techniques enable the direct fabrication of intricate three-dimensional parts from computer models,significantly enhancing production efficiency and reducing material waste[10, 11]. However, the rapid

solidification and complex thermal cycles inherent in the 3D printing process can lead to non-uniform microstructures in titanium alloys, thereby affecting their mechanical properties [12, 13]. Therefore, optimizing post-processing techniques, particularly annealing, is crucial for improving the performance of the additively manufactured TA15 titanium alloys. Oxide dispersion-strengthened (ODS) titanium alloy is an advanced material that enhances the high-temperature strength and creep resistance of titanium alloys by dispersing nanoscale oxide particles throughout the titanium matrix [14, 15]. Compared with conventional titanium alloys, ODS titanium alloys exhibit superior stability and oxidation resistance at elevated temperatures, making them highly promising for applications in high-temperature environments such as aerospace engines and nuclear energy devices [16-18]. However, research on the additively manufactured ODS titanium alloys is still in its infancy, particularly regarding the systematic investigation of the influence of annealing temperature on their microstructure and mechanical properties.

Annealing treatment is an essential post-processing step for the additively manufactured titanium alloys [19]. The annealing temperature exerts a direct influence on the microstructure of titanium alloys, encompassing grain size, phase composition, and phase distribution [20]. Moreover, proper annealing treatment can effectively release residual stresses, thereby enhancing the material's fatigue performance and resistance to stress corrosion. In recent years, numerous studies have focused on the impact of annealing temperature on the microstructure and mechanical properties of SLM-formed TA15 alloy. For instance, Huang et al. [21] conducted annealing at 800 °C on the TA15 alloy for 1 h and 4 h, respectively, and found that the elongation (EL) increased by 46.7% after heat treatment. Cai et al. [22] performed heat treatment on SLM-fabricated TA15 alloy at six different temperatures (650 °C, 750 °C, 850 °C, 950 °C, 1000 °C, and 1100 °C), with a holding time of 2 h for each. At 750 °C, a microstructure comprising acicular α' martensite, lamellar α, and nanoscale β phases was obtained. The synergistic effect of the ductile lath microstructure and the hard acicular α' martensite phase led to a favorable combination of strength and ductility. In contrast, Wang et al. [23] applied a dual heat treatment process of solution treatment (950~1100 °C/2 h/water quenching) followed by aging (600 °C/4h/air cooling) to SLM-formed TA15 alloy. After solution treatment at 1000 °C, the specimen exhibited the best overall mechanical properties, with a high-temperature ultimate tensile strength (UTS) of 715 MPa and an elongation (EL) of 24.5%. Therefore, for SLM-formed ODS titanium alloys, their unique microstructure, characterized by the dispersion of nanoscale oxide particles, means that the annealing process not only may affect the grain size of the matrix but also potentially alters the size and distribution of the oxide particles. These alterations have a direct impact on the material's room and high-temperature strength, oxidation resistance, and creep resistance.

Consequently, the present study aims to systematically investigate the influence of annealing temperature on the microstructure and mechanical properties of the additively manufactured ODS titanium alloys. By comparing the grain size, oxide particle distribution, phase composition, tensile properties, and hardness test results of the material at different annealing temperatures, this study seeks to elucidate the regulatory mechanisms of annealing temperature on the microstructure and properties of the additively manufactured ODS TA15 titanium alloys. The findings of this research are expected to provide a theoretical basis for optimizing the post-processing procedures of the additively manufactured ODS titanium alloys, thereby promoting their application in high-temperature environments.

2 Experimental section

2.1. Raw materials and preparation of composite powder

The TA15 alloy spherical powder, with a size range of 15–53 μm and supplied by Xi'an Bright Laser Technologies Co., Ltd., was produced via electrode induction gas atomization (EIGA), as depicted in Fig. 1(a).

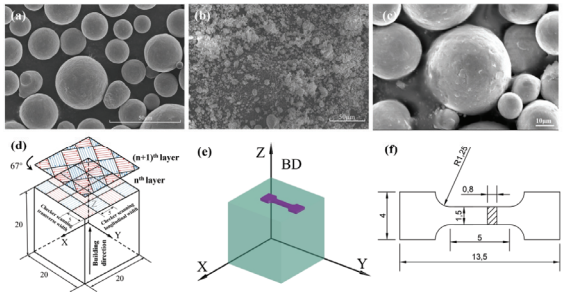

Fig. 1 The SEM images showing the morphology of the powder and schematic diagram of SLM manufacturing: (a) Original TA15 powder, (b) Original Y_2O_3 powder, (c) TA15-0.1Y_2O_3 composite powder, (d) SLM Scanning strategy, (e) Tensile sampling position, (f) Tensile specimen size.

The chemical composition is detailed in Table 1. The nano Y_2O_3 powder, with a size of 30 nm, was sourced from Beijing DK Nano Technology Co., Ltd., as shown in Fig. 1(b). The TA15-0.1Y_2O_3 (wt.%) pre-alloyed powder was milled in a PMQW4 planetary ball mill for 4 h at a rotation speed of 80 rpm (Fig. 1(c)), with a ball-to-material ratio of 1:1. The scanning electron microscope (SEM) results for the mixed pre-alloyed powders with varying compositions are illustrated in Figs. 1(a-c).

Table 1 Chemical compositions of TA15 powder (wt.%)

Element	Ti	Al	V	Zr	Mo	O
wt.%	Bal.	6.45	1.46	2.02	1.18	0.095

2.2 SLM process and heat treatment

The experimental procedure utilized TC4 substrate, and the BLT-S210 equipment, provided by Xi'an Bright Laser Technologies Co., Ltd., was employed to fabricate TA15-0.1Y_2O_3 alloys. To mitigate the oxidation of titanium alloys in elevated-temperature settings, an argon gas shield was implemented during the manufacturing process, effectively maintaining oxygen levels below 100 ppm. The experimental parameters are delineated in Table 2, with the substrate preheating temperature set at 200 °C. The scanning strategy employed was a checkerboard pattern, as depicted in Fig. 1(d). Ultimately, a block measuring 20×20×20 mm^3 was produced, achieving a relative density of 99.9%.

Table 2 Process parameters of SLM forming TA15-0.1Y_2O_3 alloy

Parameter	Unit	Value
Laser power	W	220
Scanning speed	mm/s	1050
Laser energy density	$J{\cdot}mm^{-3}$	58.2
Scanning Distance	mm	0.12
Layer thickness	μm	30
Scanning strategy		Checker mode

The conventional TA15 alloy is typically subjected to annealing within a temperature range of 700 °C to 850 °C, whereas stress-relief annealing is performed at temperatures between 600 °C and 650 °C. Given that the long-term working temperature of TA15 alloy is 500 °C, this study has selected six representative temperatures (500, 600, 700, 800, and 900 °C) for heat treatment, encompassing the temperature ranges for partial and complete decomposition of martensite, as well as the vicinity of the β phase transformation point. The heat treatment process was conducted using an OTF-1200X vacuum tube furnace (Hefei Kejing Material Technology Co., Ltd.). The heat treatment parameters are detailed in Table 3. The heating rate was set at 10 °C/min, with air serving as the cooling medium. The heat treatment process was carried out under vacuum and protected by an argon atmosphere.

Table 3 Heat treatment process parameters after SLM

Samples	HT temperature	Dwell time	Cooling mode
HT1	500 °C	4h	Air Cooling
HT2	600 °C	4h	Air Cooling
HT3	700 °C	4h	Air Cooling
HT4	800 °C	4h	Air Cooling
HT5	900 °C	4h	Air Cooling

2.3 Mechanical properties and microstructural characterization

The tensile specimen size remains consistent for both room temperature and 500 °C testing, with the sampling location and specimen dimensions depicted in Figs. 1(e-f). The room-temperature tensile testing was conducted on an AGS-X 10KN tensile testing machine, utilizing RVX-112B as a room-temperature tensile video extensometer for strain measurement. For high-temperature tensile testing, the LE5105 was employed, equipped with an LVE video extensometer to gauge strain, at a tensile rate of 5×10^{-4}/s. Subsequent to grinding with 3000-mesh sandpaper, the specimens were polished to a mirror finish and then subjected to etching in an etching solution with a ratio of HF: HNO_3: H_2O = 1:3:7. Following etching, the specimens were cleaned via ultrasonic waves for 30 min. The microstructure and fracture morphology were characterized using scanning electron microscopy (SEM, ZEISS SUPRA 40, Germany) equipped with energy dispersive spectroscope (EDS), field emission transmission electron microscopy (TEM, FEI Talos F200 X), and electron backscatter diffraction (EBSD, Nordlys Nano, OXFORD, step size 0.3 μm). Selected area electron diffraction (SAED), dark-field (DF), and bright-field (BF) modes of scanning transmission electron microscopy (STEM) are all employed in TEM. Fast Fourier transform (FFT) and

inverse fast Fourier transform (IFFT) of high-resolution transmission electron microscope (HRTEM) imaging analysis are conducted utilizing Digital Micrograph software. For TEM specimen preparation, mechanical thinning to 50 μm was followed by electrolytic thinning using a TJ100-SE-TMS double-spray instrument at -30 °C and 40 V in an electrolyte solution of 10 % perchloric acid and 90 % ethanol until perforation. The test surface of all specimens was oriented perpendicular to the build direction.

3 Results and discussion

3.1 Effect of annealing temperature on microstructure of TA15-0.1Y_2O_3 alloy

3.1.1 The microstructure of as-built TA15-0.1Y_2O_3 alloy

Fig. 2 illustrates the microstructure of TA15-0.1Y_2O_3 alloy at different annealing temperatures. As depicted in Fig. 2(a), numerous fine acicular α' martensite laths were formed within the β matrix. During the SLM process, the extremely rapid cooling rate led to the transformation of β phases into non-diffusion α' phases [24]. Concurrently, nano-scale β precipitates (indicated by arrows) emerged. These acicular or globular β phases were evenly precipitated along the martensite. Owing to the high density achieved after SLM processing, no defects were detected in the microstructure. Consequently, the microstructure of the as-built TA15-0.1Y_2O_3 sample consisted of β and α' martensite, these microstructures present a typical structure similar to what is described by Ref. [21].

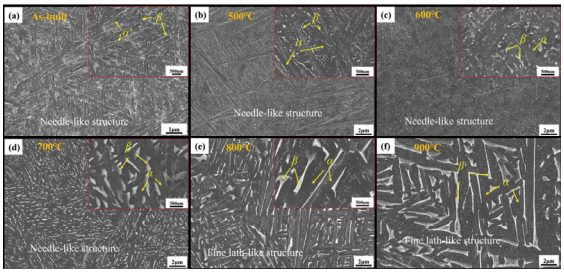

Fig. 2 Microstructure of TA15-0.1Y_2O_3 alloy at different annealing temperatures: (a) as-built; (b) 500 °C; (c) 600 °C; (d) 700 °C; (e) 800 °C; (f) 900 °C.

3.1.2 The decomposition of α' martensite and the evolution of α and β phase

As shown in Figs. 2(b-f), the microstructure of the annealed alloy consists of fine α' or α laths with β phases distributed between them. Given that the crystal structures of the α' and α phases are identical (both HCP structure with very similar lattice parameters [25]), with the α' martensite merely being a supersaturated solid solution containing higher concentrations of V and Mo, the decomposition of martensite can be assessed by integrating experimental observations with phase transformation theories [26]. Based on the phase transformation behavior of titanium alloys [27] and the current experimental results, it can be inferred that when the temperature exceeds 600°C, the α' martensite has transformed into α and β phases, with the α and β phases undergoing significant growth and coarsening as the temperature rises [28]. As the annealing temperature increases from 600 °C to 900 °C, the β phase evolves from a needle-like structure to a fine lath-like morphology. When the temperature is below 600°C, existing formulas can be employed for evaluation. The decomposition kinetics of α' phase in TA15-0.1Y_2O_3 alloy during thermal processing were quantitatively evaluated through application of the Johnson-Mehl-Avrami-Kolmogorov (JMAK) equation, a fundamental theoretical framework governing solid-state phase transformation dynamics. The mathematical representation of this kinetic model is formulated as follows [29]:

where f denotes the decomposed volume fraction of α' phase (with f = 0.99 representing 99% phase transformation completion), k_0 corresponds to the time-exponential factor (2.3×10^{12} h^{-1}), t indicates the isothermal duration (4 h in this study), Q represents the activation energy (180 $kJ\cdot mol^{-1}$), R stands for the universal gas constant (8.314 $J\cdot mol^{-1}\cdot K^{-1}$), T refers to the annealing temperature, and n signifies the Avrami exponent (n = 0.8). Numerical implementation of the JMAK framework with these kinetic parameters yields a theoretical complete decomposition temperature T ≈ 768 K (494.9 °C) for α' martensite. Nevertheless, experimental observations reveal residual α' phase persistence at 500 °C (4 h annealing), attributable to Y_2O_3 nanoparticle-induced thermal stabilization. These nanoscale dispersoids effectively suppress β phase precipitation while maintaining structural integrity. Although the initially acicular β-phase undergoes coarsening and develops discontinuous morphology during thermal exposure, its overall distribution pattern remains comparable to the pre-annealed state. This microstructural persistence strongly suggests incomplete α' phase dissolution, as residual martensitic constrain β phase evolution pathways [30].

To further discuss temperature-dependent microstructural evolution during annealing, a comparative grain morphology and orientation analysis was conducted on

typical specimens: as-built, 600 °C, and 900 °C, with corresponding analytical results presented in Fig. 3.

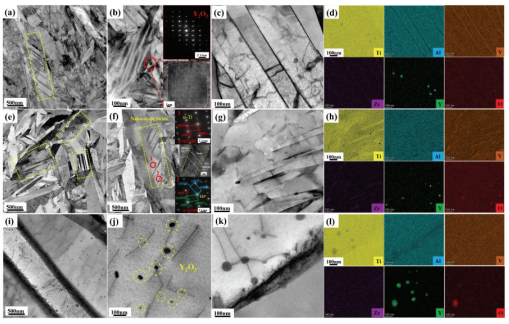

Fig. 3 The EBSD maps at different temperatures: (a-c) the IPF and the corresponding reconstructed β phase in as-built, 600 °C, and 900 °C; (d-f) the PF in As-built, 600 °C, and 900 °C.

Compared with the as-built condition, where the average grain sizes of the α' and β phases are 2.18 μm and 6.73 μm, respectively, the α' phase decomposes into the α phase after annealing at 600 °C, and the average grain sizes of the α and β phases increase to 2.32 μm and 7.90 μm, respectively. Following annealing at 900 °C, the α and β phases further grow to 2.42μm and 8.22 μm, respectively. Additionally, the texture index rises from 13.34 to 13.64, and then to 19.4 at 900 °C (Fig. 3(d-f)). Judging from the extent of grain size increment, the presence of Y_2O_3 nanoparticles may pin the grain boundaries, thereby retarding the tendency of grain growth [31]. Regarding textural development, differential thermal activation manifests distinct governing principles across temperature regimes. At the lower annealing threshold (600 °C), limited thermal energy results in sluggish grain boundary mobility. Concurrently, Y_2O_3 nanoparticles demonstrate effective suppression of preferentially oriented grains inherited from additive manufacturing processes. This restricted growth anisotropy consequently maintains near-baseline texture intensity, with minimal enhancement in texture index [32]. In contrast, elevated temperature (900 °C) initiates pronounced isotropic coarsening, yet comparative analysis reveals higher texture intensity than 600 °C annealed counterparts. This apparent paradox resolves through identification of anisotropic growth constraints. Although grains grow in all directions, the growth in some directions is still hindered by Y_2O_3 nanoparticles. Therefore, the texture index is significantly higher than that of the sample annealed at 600 °C.

3.1.3 The evolution of nanotwins and Y_2O_3 nanoparticles

To gain a deeper understanding of the influence of Y_2O_3 nanoparticles on the microstructural evolution under various annealing temperatures, TEM characterization was performed on samples in the as-built condition as well as those annealed at 600 °C and 900 °C, as shown in Fig. 4.

Apart from the α′ martensites, several parallel twins with nanoscale thickness (yellow dashed box) could be distinctly observed (Fig. 4(a)) in the as-built alloy. The formation of nanotwins predominantly originates from non-equilibrium phase transformation dynamics during rapid solidification, where β→α' martensitic transition occurs under high cooling rates [19, 33, 34]. This extreme thermal gradient induces substantial lattice distortion and phase transformation-induced stress concentration, subsequently triggering nanotwins nucleation through displacive mechanisms [22]. Due to the combined effects of lattice distortion and stress, a certain number of dislocations exist within both the matrix and the twins, and pile-ups occur at the phase interfaces, with severe distortion regions exhibiting indistinct phase boundary. Notably, the Y_2O_3 nanoparticles are also distributed throughout the matrix and at the interfaces, and the TEM result provides direct evidence of dislocation-nanoparticle interactions, where Y_2O_3 dispersoids effectively pin mobile dislocations (Fig. 4 (b-d)) through Orowan strengthening mechanisms [35].

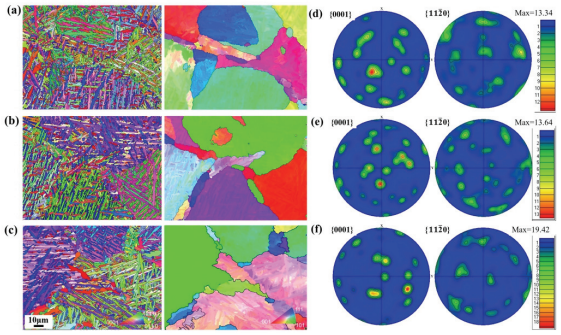

Fig. 4 TEM images of TA15-0.1Y_2O_3 alloy annealed at different temperatures: (a-d) the BF, SAED, and EDS images of as-built; (e-h) the BF, SAED, HRTEM, and EDS images at 600 °C annealing; (i-l) the BF and EDS images at 900 °C annealing.

The distinct microstructural responses to thermal processing emerge through comparative analysis of 600 °C and 900 °C annealing TEM results. Following thermal treatment at 600 °C, homogenization of the matrix architecture becomes evident, accompanied by reduction in dislocation density (Fig. 4(e)). Enhanced twin density (yellow dashed box) within α phases suggests stress redistribution mechanisms, with residual dislocations preferentially confined to twin interiors. While α phase domains exhibit moderate coarsening, Y_2O_3 nanoparticles maintain

dimensional stability without detectable growth (Fig. 4(d) and (h)). Annealing at 600 ℃ induces common thermodynamically driven dislocation slip, climb, and reconfiguration behaviors, resulting in a reduction in dislocation density, an increase in grain size, and a tendency toward microstructural homogenization. However, an anomalous increase in the number of twins is also observed, as the twins formed in titanium alloys are typically unstable at high temperatures [36]. From the perspectives of microstructure and energy, studies have demonstrated that titanium alloys prepared by laser powder bed fusion (LPBF) with high-density screw dislocation configurations can form nanotwins after heat treatment at 480 ℃ for 6 h [37]. Researchers believe that the high density of dislocations provides the foundation for the formation of nanotwins during subsequent heat treatment. During the heat treatment process, atoms within the material gain energy, which significantly reduces the energy barrier required for nucleation of precipitated phases around dislocation cores. This facilitates the formation of new phases or structures, namely nanotwins, around the dislocations. Additionally, dislocations rearrange and migrate to the vicinity of twin boundaries, and the migration of twin boundaries is impeded by Y_2O_3, which has higher thermal stability. This can further enhance their stability [38]. In stark contrast, 900 ℃ annealing induces threefold microstructural variations: (i) Accelerated phase coarsening with α phases thickening and β phase expanding (Fig. 4(i)); (ii) Dislocation annihilation reducing defect density, residual dislocations forming Orowan loops around Y_2O_3 particles (Fig. 4(j-k)); (iii) Complete dissolution of nanotwins coupled with nanoparticle coarsening (Fig. 4(l)). Annealing at 900 ℃ can eliminate the vast majority of dislocations and induce significant grain coarsening. Meanwhile, the intensified atomic motion at high temperatures leads to a substantial decrease in the stability of nanotwins. During the Ostwald ripening process, grain growth consumes a large number of interfaces, thereby reducing the number of nanotwins or even causing detwinning [39].

3.2 Effect of annealing temperature on mechanical properties of TA15-0.1Y_2O_3 alloy

3.2.1 Effect of annealing temperature on room temperature mechanical properties

Fig. 5 presents the room-temperature tensile engineering stress-strain curves of TA15-0.1Y_2O_3 alloy at different annealing temperatures, along with the corresponding ultimate tensile strength (UTS), yield strength (YS), and elongation (EL).

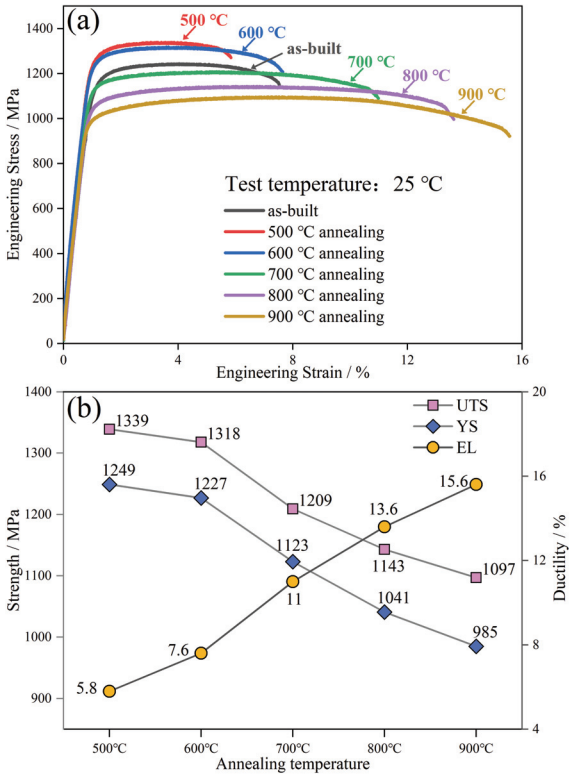

Fig. 5 Tensile properties of TA15-0.1Y_2O3 alloy at 25 ℃: (a) engineering stress-strain curves at different annealing temperatures: (b) comparison of mechanical properties (UTS, YS and EL) at different annealing temperatures.

Compared with the as-built alloy, annealing at 500 °C enhanced the YS from 1146 MPa to 1249 MPa (a 9% increase) and UTS from 1244 MPa to 1339 MPa (a 7.6% improvement), while reducing EL from 7.5% to 5.8%. Upon annealing at 600 °C, the UTS slightly decreased to 1318 MPa but remained superior to that of the as-built counterpart, with EL exhibiting comparable values to the unannealed state. Notably, when the annealing temperature exceeded 600 °C, a progressive decline in strength parameters was observed, inversely correlated with a marked elevation in ductility. These results demonstrate that the mechanical properties of TA15-0.1Y_2O_3 alloy exhibit a temperature-dependent transition.

The observed non-monotonic evolution of tensile properties aligns with distinct microstructural transformation stages, which can be categorized into two characteristic states: fully martensitic structures (as exemplified by the as-built alloy) and fully decomposed martensitic architectures (typified by the 600°C-annealed and 900°C-annealed sample). The fully martensitic structure deforms through interactions between dislocations and nanotwins, where the fine hard/brittle

martensitic phase and nanotwin boundaries act as potent obstacles to dislocation glide [40]. This obstruction mechanism induces significant dislocation density accumulation, exacerbating pre-existing localized stress concentrations at interfaces inherent in the as-built alloy [41]. Consequently, premature fracture occurs in the as-built alloy, evidenced by fracture surfaces exhibiting quasi-cleavage characteristics with limited dimples containing embedded Y_2O_3 particles, as shown in Fig. 6(a-c). These observations suggest that stress concentration predominantly initiates at matrix/Y_2O_3 interfaces, where micro-void nucleation and coalescence drive crack propagation.

Upon annealing at 600°C, the microstructure transitions to complete martensite decomposition structure comprising α and β phases, accompanied by increased nanotwin density. The strength enhancement arises predominantly from interface strengthening provided by this multiphase architecture [42], while the marginal ductility improvement correlates with reduced dislocation density and enhanced plastic strain accommodation enabled by proliferated nanotwins [43]. Fractographic analysis reveals dominant cleavage features, including cleavage planes and terraces (Fig. 6(d-f)), indicative of brittle-dominated fracture mechanisms.

When annealed at 900°C, complete martensite decomposition yields a microstructure dominated by α and β phases. The dramatic reduction in dislocation density, disappearance of multiphase interfaces, and pronounced microstructural coarsening collectively confer exceptional ductility but substantially diminished strength. This inverse strength-ductility relationship underscores the critical balance between defect-mediated strengthening mechanisms and thermally activated microstructure evolution during post-processing treatments.

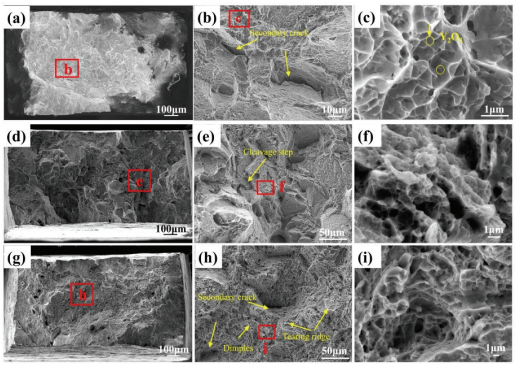

Fig. 6 The tensile fracture morphology of TA15-0.1Y_2O_3 alloy at 25 ℃: (a-c) As-built; (d-f) 600°C annealing; (g-h) 900°C annealing.

3.2.2 Effect of annealing temperature on 500 °C mechanical properties

Fig. 7 presents the 500°C tensile properties of TA15-0.1Y_2O_3 alloy at different annealing temperatures.

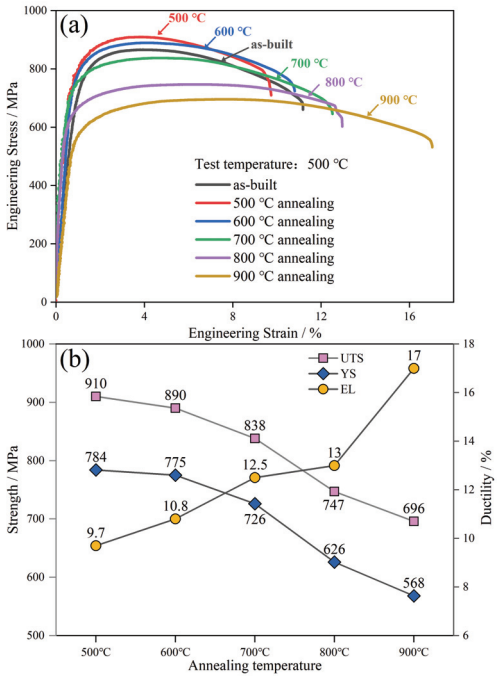

Fig. 7 Tensile properties of TA15-0.1Y_2O_3 alloy at 500 ℃: (a) engineering stress-strain curves at different annealing temperatures; (b) comparison of mechanical properties (UTS, YS and EL) at different annealing temperatures.

The tensile properties of TA15-0.1Y_2O_3 alloy at 500 °C show a similar trend to those at room temperature. When the annealing temperature is less than or equal to 600 °C, the strength is higher than that of the as-built alloy, while the elongation remains comparable. However, when the annealing temperature exceeds 600 °C, the alloy's strength gradually decreases, especially after the annealing temperature surpasses 700 °C, where a more pronounced decline in strength is observed. The strength of titanium alloys typically exhibits a progressive decline with increasing tensile temperature [44], a phenomenon attributable to thermally activated atomic motion [45]. Elevated temperatures enhance atomic mobility, thereby reducing the resistance to dislocation motion and facilitating material deformation [46]. Conventionally, the yield strength of polycrystalline materials at ambient temperature adheres to the Hall-Petch relationship, where diminished grain dimensions correlate with enhanced mechanical strength. Notably, this relationship remains valid for the investigated specimens even under elevated temperatures of 500°C, demonstrating the persistence of grain-boundary strengthening mechanisms despite thermal activation effects [47]. These observations

underscore the interplay between thermal energy input and microstructural constraints in governing the temperature-dependent mechanical behavior of titanium alloys [48]. Unlike the room-temperature tensile behavior, at 500 °C, the as-received fracture surface exhibited increased tortuosity, the cleavage features after annealing at 600 °C were significantly reduced, and the fracture surface after annealing at 900 °C displayed numerous grooves, as shown in Fig. 8.

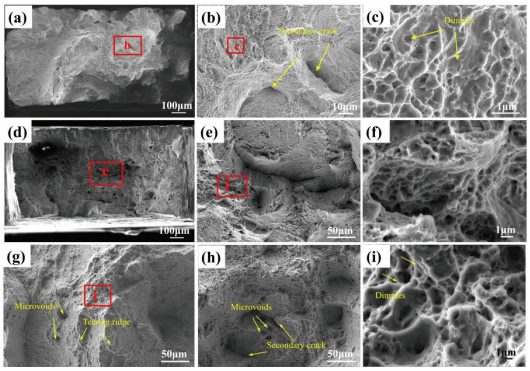

Fig. 8 The tensile fracture morphology of TA15-0.1Y_2O_3 alloy at 500 ℃: (a-c) As-built; (d-f) 600°C annealing; (g-h) 900°C annealing.

4 Conclusions

Annealing temperature critically governs phase evolution (α′→α+β) and mechanical properties in SLM-fabricated TA15-Y_2O_3. Y_2O_3 stabilizes nano-twins below 600°C, enhancing strength, while higher temperatures promote β-coarsening and ductility. Optimal 600°C annealing achieves balanced UTS (1318 MPa) and EL (7.65%). Y_2O_3 nanoparticles uniquely delay α′ decomposition and suppress β-phase precipitation, enabling dual-phase stabilization. This introduces a novel strategy for tailoring strength-ductility trade-offs via oxide dispersion-mediated microstructural control. Further exploration of multi-stage annealing protocols and synergistic effects of alternative oxide additives s recommended. In-situ studies during thermal cycling could elucidate dynamic phase transformation mechanisms, while long-term high-temperature stability assessments are essential for aerospace applications.

Acknowledgments

This work was supported by the National Science and Technology Major Project (Grant Nos. 2024ZD0706401) and the National Natural Science Foundation of China (Grant Nos. 12265008).

Conflicts of interest

Authors declare that they have no conflict of interest.

References

[1] Wang S, Yang J, Sun J, et al., Tensile properties of Ti6.5Al2Zr1Mo1V titanium alloy fabricated via electron beam selective melting at high temperature, Mater. Sci. Eng, A.,2023,888:145806.

[2] Sefene E M, State-of-the-art of selective laser melting process: A comprehensive review, J. Manuf. Syst.,2022,63:250-274.

[3] Zhu Y, Zeng W, Zhao Y, et al., Effect of processing parameters on hot deformation behavior and microstructural evolution during hot compression of Ti40 titanium alloy, Mater. Sci. Eng, A.,2012,552:384-391.

[4] Banerjee D, Williams J C, Perspectives on Titanium Science and Technology, Acta Mater.,2013,61(3):844-879.

[5] Zhao J, Lv L, Wang K, et al., Effects of strain state and slip mode on the texture evolution of a near-α TA15 titanium alloy during hot deformation based on crystal plasticity method, J. Mater. Sci. Technol.,2020,38:125-134.

[6] Pothala S, Jagannadha Raju M V, Recent advances of metallic bio-materials in additive manufacturing in biomedical implants–A review, Mater. Today: Proce.,2023,07:109843.

[7] Gao P F, Yang H, Fan X G, et al., Microstructural features of TA15 titanium alloy under different temperature routes in isothermal local loading forming, Mater. Sci. Eng, A.,2012,540:245-252.

[8] Madigana C S, Vaddula A, Yerramsetti S D, et al., Additive manufacturing of titanium and nickel- based superalloys: A review, Mater. Today: Proce.,2023,07:082556.

[9] Li K, Yang T, Gong N, et al., Additive manufacturing of ultra-high strength steels: A review, J. Alloys. Compd.,2023,965:171390.

[10] Alipour S, Moridi A, Liou F, et al., The Trajectory of Additively Manufactured Titanium Alloys with Superior Mechanical Properties and Engineered Microstructures, Addit. Manuf.,2022,60:103245.

[11] Li N, Huang S, Zhang G, et al., Progress in additive manufacturing on new materials: A review, J. Mater. Sci. Technol.,2019,35(2):242-269.

[12] Yu A, Zhang C, Xu W, et al., Additive manufacturing of multi-morphology graded titanium scaffolds for bone implant applications, J. Mater. Sci. Technol.,2023,139:47-58.

[13] Zhang D, Qiu D, Gibson M A, et al., Additive manufacturing of ultrafine-grained high-strength titanium alloys, Nature,2019,576(7785):91-95.

[14] Wilms M B, Rittinghaus S-K, Gossling M, et al., Additive manufacturing of oxide-dispersion strengthened alloys: Materials, synthesis and manufacturing, Prog. Mater. Sci.,2023,133:101049.

[15] Gao Z, Bu H, Feng Y, et al., Strengthening mechanism of

Y_2O_3 nanoparticles on microstructure and mechanical properties of the laser additive manufacturing joint for large thickness TC4 titanium alloy, J. Manuf. Processes,2021,71:37-55.

[16] Liu Y, Song Z, Guo Y, et al., Simultaneously enhancing strength and ductility of LPBF Ti alloy via trace Y_2O_3 nanoparticle addition, J. Mater. Sci. Technol.,2024,191:146-156.

[17] Guo Y, Xiao S, Chen Y, et al., High temperature tensile properties and fracture behavior of Y_2O_3-bearing Ti-48Al-2Cr-2Nb alloy, Intermetallics,2020,126:106933.

[18] Lu K, The Future of Metals, Science,2010,328(5976):319-320.

[19] Jiang J, Ren Z, Ma Z, et al., Mechanical properties and microstructural evolution of TA15 Ti alloy processed by selective laser melting before and after annealing, Mater. Sci. Eng, A.,2020,772:138742.

[20] Sun Z, Mao X, Wu H, et al., Tri-modal microstructure and performance of TA15 Ti-alloy under near-β forging and given subsequent solution and aging treatment, Mater. Sci. Eng, A.,2016,654:113-123.

[21] Huang S, Sun B, Guo S, Microstructure and property evaluation of TA15 titanium alloy fabricated by selective laser melting after heat treatment, Opt. Laser Technol.,2021,144:107422.

[22] Cai C, Wu X, Liu W, et al., Selective laser melting of near-α titanium alloy Ti-6Al-2Zr-1Mo-1V: Parameter optimization, heat treatment and mechanical performance, J. Mater. Sci. Technol.,2020,57:51-64.

[23] Wang Q, Jin B, Zhao L, et al., Microstructural Evolution and Mechanical Behavior of TA15 Titanium Alloy Fabricated by Selective Laser Melting: Influence of Solution Treatment and Aging, Metals,2023,13(9):1514.

[24] Qiu C, Adkins N J E, Attallah M M, Microstructure and tensile properties of selectively laser-melted and of HIPed laser-melted Ti–6Al–4V, Mater. Sci. Eng, A.,2013,578:230-239.

[25] Chlebus E, Kuźnicka B, Kurzynowski T, et al., Microstructure and mechanical behaviour of Ti—6Al—7Nb alloy produced by selective laser melting, Mater. Charact.,2011,62(5):488-495.

[26] Zhang Y, Zhai Z, Wu Z, et al., Tailoring high-temperature mechanical properties of laser powder bed fusion Ti-6.5Al-2Zr-1Mo-1 V alloy via microstructure design, Materials & Design,2023,236:112488.

[27] Wang S, Zhang R, Ji M, et al., Microstructure evolution and enhanced mechanical properties of as-rolled TiB/(TA15-Si) composite via heat treatment, Mater. Sci. Eng, A.,2024,890:145888.

[28] Ci S, Hu J, Cheng Z, et al., Impact of Hot Isostatic Pressing Temperature on Tensile Properties of TA15 Titanium Alloy Produced via Laser Powder Bed Fusion, Coatings,2023,13(10):1742.

[29] Lei X, Huang J, Jin X, et al., Application of Johnson-Mehl-Avrami-Kolmogorov type equation in non-isothermal phase process: Re-discussion, Mater. Lett.,2016,181:240-243.

[30] Kaschel F R, Vijayaraghavan R K, Shmeliov A, et al., Mechanism of stress relaxation and phase transformation in additively manufactured Ti-6Al-4V via in situ high temperature XRD and TEM analyses, Acta Mater.,2020,188:720-732.

[31] Ben-fu H U, Li-na G U O, Shun-mi P, et al., Mechanism of forming strengthening phase (Y_2O_3) in oxide dispersion strengthened steels produced by a chemical method, Chinese Journal of Engineering,2011,33(3):308-312.

[32] Wei G, Li S, Chen Y, et al., Annealing characteristics and mechanism interpretation of high-performance swaged W-Y2O3 alloy, Int. J. Refract. Met. H.,2024,124:106838.

[33] Wu X, Cai C, Yang L, et al., Enhanced mechanical properties of Ti-6Al-2Zr-1Mo-1V with ultrafine crystallites and nano-scale twins fabricated by selective laser melting, Mater. Sci. Eng, A.,2018,738:10-14.

[34] Wang J, Zhu R, Liu Y, et al., Understanding melt pool characteristics in laser powder bed fusion: An overview of single- and multi-track melt pools for process optimization, Adv. Powder Mater.,2023,2(4):100137.

[35] Kombaiah B, Murty K L, Coble, Orowan Strengthening, and Dislocation Climb Mechanisms in a Nb-Modified Zircaloy Cladding, Metall. Mater. Trans. A,2015,46(10):4646-4660.

[36] Yan F K, Wang Y, Lu W J, et al., Nanolamellar and ultrafine equiaxed (α + β) phase heterogeneously architected by nanotwins in a twinning-induced plasticity Ti-12Mo alloy, Acta Mater.,2025,288:120844.

[37] Zhu Y, Zhang K, Meng Z, et al., Ultrastrong nanotwinned titanium alloys through additive manufacturing, Nat. Mater.,2022,21(11):1258-1262.

[38] Zhao S, Zhang R, Yu Q, et al., Cryoforged nanotwinned titanium with ultrahigh strength and ductility, Science,2021,373(6561):1363-1368.

[39] Lin Y, Zhang Z, Duan F, et al., Full-Scaling Friction and Wear Laws of Nanotwinned Metals, Phys. Rev. Lett.,2025,134(16):166201.

[40] Qu Z, Zhang Z J, Zhu Y K, et al., Coupling effects of microstructure and defects on the fatigue properties of laser powder bed fusion Ti-6Al-4V, Additive Manufacturing,2023,61:103355.

[41] Zhu Y, Wang C, Liang M, et al., Effect of annealing temperature on the microstructure and mechanical properties of Al15Ti35V20Nb15Zr15 alloy, Int. J. Refract. Met. H.,2025,130:107154.

[42] Liu C, Ye J, Wei X, et al., Strength-ductility synergy in 3D-printed (TiB + TiC)/Ti6Al4V composites with unique dual-heterogeneous structure, Compos. Part B: Eng.,2023,266:111008.

[43] Wang Q, Wang M, Guo S, et al., In situ tensile test of selective laser melted Ti-6.5Al-2Zr-1Mo-1V alloy at different stages of martensite decomposition, J. Mater. Sci. Technol.,2023,58(4):1798-1812.

[44] Wang C, Qin H, Ma L, et al., Enhanced tensile properties of laser powder-bed fusion-manufactured TA15 alloy across a wide temperature range, Mater. Sci. Eng, A.,2025,926:147950.

[45] Li S, Li S, Liu L, et al., High-temperature “Inverse” Hall-Petch relationship and fracture behavior of TA15 alloy, Int. J. Plasticity,2024,176:103951.

[46] Li S, Li S, Liu L, et al., High temperature softening mechanism of powder metallurgy TA15 alloy, Mater. Sci. Eng, A.,2023,877:145160.

[47] Chuan W, He Y, wei L H, Substructure and texture evolution and flow behavior of TA15 titanium alloy compressed in the alpha+beta two-phase field, J. Mater. Process. Technol.,2013,213(11):2033-2041.

[48] Ning Y Q, Luo X, Liang H Q, et al., Competition between dynamic recovery and recrystallization during hot deformation for TC18 titanium alloy, Mater. Sci. Eng, A.,2015,635:77-85.